

# Perovskite–Erbium Silicate Nanosheet Hybrid Waveguide Photodetectors at the Near-Infrared Telecommunication Band

Xuehong Zhang, Shuzhen Yang, Hong Zhou, Junwu Liang, Huawei Liu, Hui Xia, Xiaoli Zhu, Ying Jiang, Qinglin Zhang, Wei Hu, Xiujuan Zhuang, Hongjun Liu, Weida Hu, Xiao Wang, and Anlian Pan\*

Methylammonium lead halide perovskites have attracted enormous attentions due to their superior optical and electronic properties. However, the photodetection at near-infrared telecommunication wavelengths is hardly achievable because of their wide bandgaps. Here, this study demonstrates, for the first time, novel perovskite–erbium silicate nanosheet hybrid photodetectors with remarkable spectral response at  $\approx 1.54 \mu\text{m}$ . Under the near-infrared light illumination, the erbium silicate nanosheets can give strong upconversion luminescence, which will be well confined in their cavities and then be efficiently coupled into and simultaneously excite the adjacent perovskite to realize photodetection. These devices own prominent responsivity and external quantum efficiency as high as previously reported microscale silicon-based sub-bandgap photodetectors. More importantly, the photoresponse speed ( $\approx 900 \mu\text{s}$ ) is faster by five orders than the ever reported hot electron silicon-based photodetectors at telecommunication wavelengths. The realization of perovskite-based telecommunication band photodetectors will open new chances for applications in advanced integrated photonics devices and systems.

all kinds of advanced devices have been fabricated based on perovskite materials, including highly efficient solar cells, high quantum yields light-emitting diodes, high-quality lasers, and so forth.<sup>[2–5]</sup> Importantly, perovskite-based photodetectors have also been widely developed with excellent performances.<sup>[6,7]</sup> Unfortunately, the reported perovskite-based detectors mainly work at the visible spectral region, limited by the intrinsic bandgap of  $\approx 1.5 \text{ eV}$ .<sup>[8]</sup> Developing perovskite based infrared (IR) photodetectors is important for their potential applications in biodelecting, IR imaging technology, and information communication.<sup>[9]</sup> However, to our best knowledge, perovskite-based infrared light detection at the near-IR communication band has never been achieved. It is well-known that rare earth (RE) erbium ions own upconversion (UC) light emission and can be used to detect infrared

Recently, methylammonium lead halide perovskites have emerged as promising optoelectronic materials mainly due to their facile fabrication, low-cost, and excellent optoelectronic properties, such as direct bandgap, large absorption coefficient, low noise currents, and long carrier diffusion length.<sup>[1]</sup> To date,

photons because of their rich discrete energy level structure that allows efficient capturing of infrared light at the telecommunication region.<sup>[10–13]</sup> Highly efficient infrared photoresponses have been reported in RE-semiconductor heterostructures.<sup>[14–18]</sup> For instance, He and co-workers realized the efficient spectral absorption of perovskite solar cells at near-infrared wavelength using upconversion nanoparticles.<sup>[19]</sup> On the other hand, waveguide-based hybrid optoelectronic devices have attracted great deal of attentions and interests owing to the substantial light absorption enhancement derived from the waveguide cavity.<sup>[20–28]</sup> In these hybrid devices, the efficient light confinement and propagation capabilities of the waveguide cavity as well as multiple opportunities for energy transfer at the interfaces significantly improve the photoresponsivity, which paves the way for many advanced device applications such as photodetectors and photovoltaics.

In this work, a kind of single-crystalline erbium ytterbium silicate (EYS) nanosheets have been achieved, which can give high-efficient UC visible light emission under the illumination of near-infrared light, and simultaneously act as high-quality microscale waveguide cavity to confine and propagate the emitted UC light. By conveniently combining the achieved individual EYS nanosheets with high-quality perovskite thin film, for the first time, we have fabricated a novel perovskite–EYS nanosheet hybrid waveguide photodetector architecture,

X. H. Zhang, S. Z. Yang, Dr. H. Zhou, H. W. Liu, Dr. X. L. Zhu, Dr. Y. Jiang, Prof. Q. L. Zhang, Dr. W. Hu, Prof. X. J. Zhuang, Prof. H. J. Liu, Prof. X. Wang, Prof. A. L. Pan  
Key Laboratory for Micro-Nano Physics and Technology of Hunan Province  
College of Physics and Electronics  
State Key Laboratory of Chemo/Biosensing and Chemometrics  
Hunan University  
Changsha 410082, P. R. China  
E-mail: anlian.pan@hnu.edu.cn  
Prof. J. W. Liang  
School of Physical Science and Technology Engineering  
Yulin Normal University  
Yulin 537000, P. R. China  
Dr. H. Xia, Prof. W. D. Hu  
National Laboratory for Infrared Physics  
Shanghai Institute of Technical Physics  
Chinese Academy of Sciences  
Shanghai 200083, China



DOI: 10.1002/adma.201604431

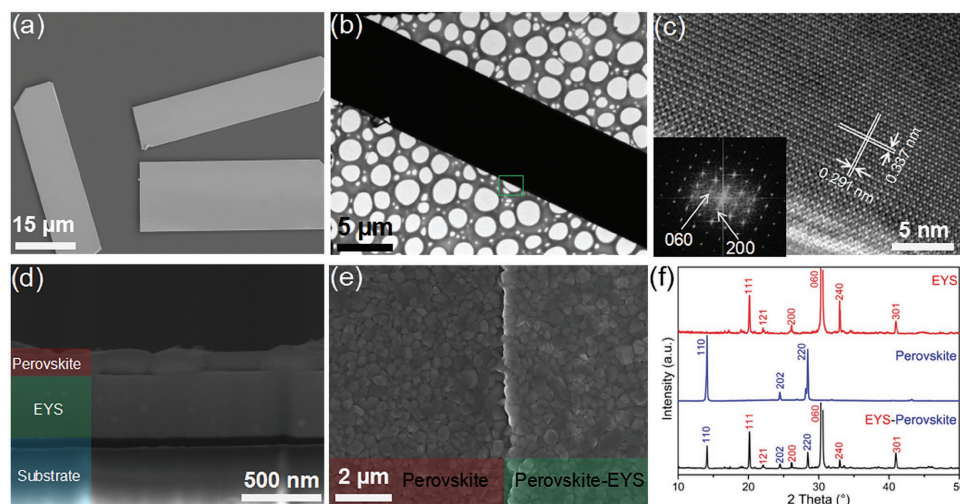


**Figure 1.** Morphology and structure of EYS nanosheet and perovskite thin film. a) SEM image of the EYS nanosheets. b) Typical TEM image of an individual nanosheet. c) Enlarged lattice-resolved HRTEM image taken from the marked area in (b). The inset shows the corresponding FFT pattern. d) Cross-sectional and e) top view SEM images of the perovskite–EYS hybrid. f) XRD patterns for EYS nanosheet, perovskite, and perovskite–EYS hybrid.

which exhibits significant photoresponse at the near-infrared telecommunication wavelengths ( $\approx 1.54 \mu\text{m}$ ) due to the efficient energy transfer from the EYS waveguide cavity to the perovskite film. The hybrid devices demonstrate significantly improved near-infrared photoresponse as compared with the pristine perovskite, and the achieved photoresponsivity is as high as the widely reported microscale silicon-based photodetectors at the same spectral region even at low driving voltages.<sup>[29–36]</sup> More importantly, the present photodetectors show superior photoswitching characteristics and a response time of  $\approx 900 \mu\text{s}$  which is faster by five orders than those of the silicon-based hot electron photodetectors,<sup>[31–36]</sup> and by one to three orders than most other nonavalanche semiconductor photodetectors at telecommunication wavelengths reported so far.<sup>[37–44]</sup> With the advantages of low cost, facile fabrication, and superior performance, the developed microscale perovskite–EYS hybrid telecommunication photodetectors may act as a promising candidate for advanced on-chip integrated optoelectronic applications.

EYS nanosheets were first grown using an improved chemical vapor deposition route.<sup>[45]</sup> **Figure 1a** shows a typical scanning electron microscopy (SEM) image of the 2D nanosheets with smooth surface, rectangular shape, size up to a few tens of micrometers, and thickness of  $\approx 400 \text{ nm}$ . The size of the nanosheet can be tuned via controlling the growth directions. The crystal structures were studied by transmission electron microscopy (TEM). **Figure 1b** shows the TEM image of a single EYS nanosheet with a width of  $\approx 10 \mu\text{m}$ . **Figure 1c** gives the high-resolution TEM (HRTEM) image and the corresponding fast Fourier transform (FFT) (inset), which validates the single-crystalline nature of the as-grown EYS nanosheets. The two sets of lattice fringes along and perpendicular to the longitudinal axis of the nanosheet are  $0.291$  and  $0.337 \text{ nm}$ , respectively, corresponding to the (060) and (200) planes of orthorhombic structure of  $(\text{Er}/\text{Yb})_3\text{Cl}(\text{SiO}_4)_2$ .

Perovskite–EYS nanosheet hybrid structures were fabricated by depositing perovskite film onto individual EYS nanosheets. First, the EYS nanosheets were transferred onto a  $\text{SiO}_2$  or

$\text{SiO}_2/\text{Si}$  substrate. A layer of  $\text{PbI}_2$  film with a thickness of  $\approx 80 \text{ nm}$  was deposited on these nanosheets by thermal evaporation. Then  $\text{CH}_3\text{NH}_3\text{I}$  solution was spin-coated onto the  $\text{PbI}_2$  layer, followed by a postannealing process to form  $\text{CH}_3\text{NH}_3\text{PbI}_3$  perovskite layer. **Figure 1d** shows the cross-sectional view of the perovskite–EYS nanosheet hybrid structure, which indicates that the perovskite film is successfully deposited onto the EYS nanosheet. In addition, the thicknesses of EYS nanosheet and perovskite film are found to be  $\approx 400$  and  $\approx 190 \text{ nm}$ , respectively. Top view SEM image (**Figure 1e**) of the perovskite film on EYS nanosheets appears relatively smooth surface without pinholes, and the uniform grains have sized up to hundreds of nanometers. As shown in **Figure 1f**, the peaks in the X-ray diffraction (XRD) pattern of pristine EYS nanosheets can all be indexed to the orthorhombic structure of  $(\text{Er}/\text{Yb})_3\text{Cl}(\text{SiO}_4)_2$ ,<sup>[46]</sup> which is consistent with the energy-dispersive X-ray (EDX) spectrum of the nanosheet (**Figure S1**, Supporting Information). The perovskite shows three main peaks at  $14.08^\circ$ ,  $24.46^\circ$ , and  $28.44^\circ$ , which can be assigned to the (110), (202), and (220) crystallographic planes of  $\text{CH}_3\text{NH}_3\text{PbI}_3$ , respectively.<sup>[47,48]</sup> In the perovskite–EYS nanosheet hybrid, the characteristic diffraction peaks of both perovskite and EYS are observed, further indicating that the perovskite–EYS nanosheet hybrids were fabricated successfully.

The energy transfer from EYS nanosheet to perovskite film was revealed through in situ photoluminescence (PL) measurements of the pristine EYS nanosheet and perovskite–EYS hybrid under excitation at  $1530 \text{ nm}$ . **Figure 2a** shows the PL and absorption spectra of the perovskite thin film. The PL emission peak is located at  $\approx 771 \text{ nm}$ , which agrees well with the typical value reported in the literature.<sup>[49]</sup> It is also observed that the perovskite thin film is capable of absorbing photons with wavelengths covering the entire visible light spectrum, while seldom of the photons can be absorbed with wavelengths less than  $800 \text{ nm}$ . To this end, the perovskite materials can hardly be recognized as the promising candidate for infrared communication detection applications. Nonetheless, under infrared

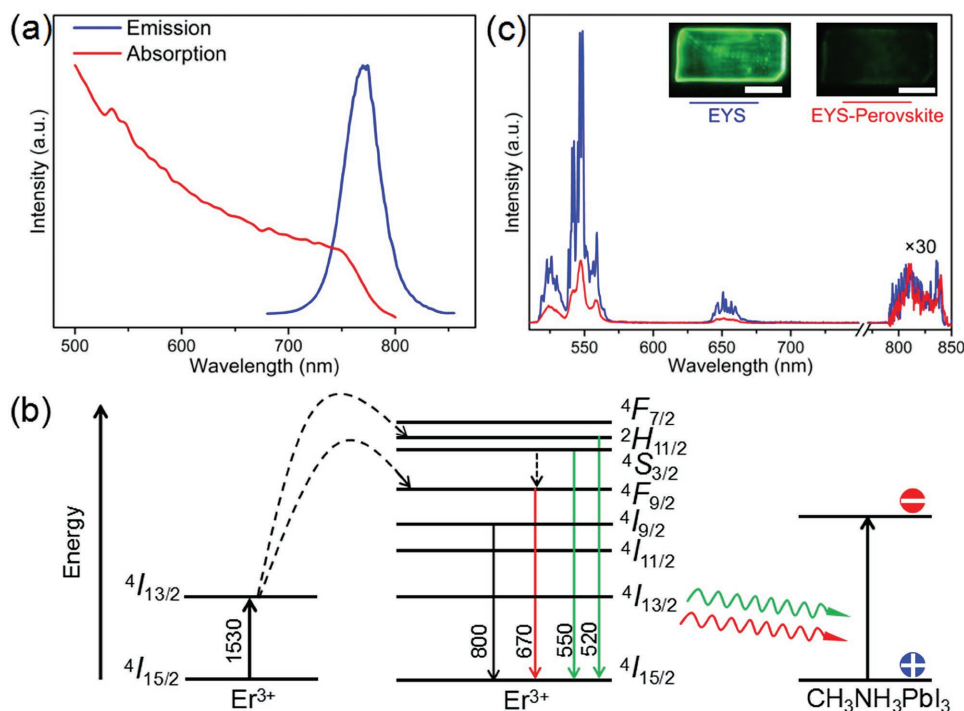


**Figure 2.** Radiative energy transfer of the perovskite–EYS hybrid. a) Emission and absorption spectra of the perovskite thin film. b) Energy level and the radiative energy transfer. c) Emission spectra of the pristine EYS nanosheet and perovskite–EYS hybrid. The PL located at 800 nm was enlarged 30 folds. The insets show the corresponding optical images. All the scale bars: 10  $\mu\text{m}$ .

illumination at 1530 nm, the EYS nanosheet shows four characteristic Er<sup>3+</sup> upconverted emission peaks at 520, 550, 670, and 800 nm (due to  $^2\text{H}_{11/2} \rightarrow ^4\text{I}_{15/2}$ ,  $^4\text{S}_{3/2} \rightarrow ^4\text{I}_{15/2}$ ,  $^4\text{F}_{9/2} \rightarrow ^4\text{I}_{15/2}$ , and  $^4\text{I}_{9/2} \rightarrow ^4\text{I}_{15/2}$ , respectively<sup>[12]</sup>), as shown in Figure 2b. The upconverted emission property of the EYS nanosheet entails the infrared communication detection via the marriage of EYS nanosheet and perovskite materials, through which the infrared signals can be upconverted to visible ones and be detected by perovskite materials. Figure 2c shows the PL spectra of both the pristine EYS nanosheet and the perovskite–EYS hybrid. A color charge-coupled device (CCD) image of EYS nanosheet (inset of Figure 2c) exhibits intense green emission with bright emission at the sheet edges, indicating the good optical waveguide cavity for efficiently confining and transporting light,<sup>[50]</sup> which can be clearly observed through exciting the center of the nanosheet (Figure S2, Supporting Information). As a contrast, a remarkable reduction of the two short-wavelength emission bands of Er<sup>3+</sup> at 520 and 550 nm by  $\approx 60\%$  is observed for the perovskite–EYS hybrid compared to that of the pristine EYS nanosheet, which is also revealed by the corresponding CCD image (inset of Figure 2c). The emission peak of Er<sup>3+</sup> at 800 nm shows no clearly difference between EYS nanosheet and perovskite–EYS hybrid, which is consistent with the absorption spectra shown in Figure 2a. This phenomenon suggests a strong energy transfer through direct luminescence quenching by perovskite materials, as reported previously.<sup>[17]</sup>

To further reveal the energy transfer process from EYS nanosheet to perovskite, PL propagation loss measurements of the EYS nanosheet and perovskite–EYS hybrid structure have been performed using a confocal optical microscope setup

with separately controlled excitation and collection objectives. As depicted in Figure 3a, an EYS nanosheet with the length of  $\approx 60 \mu\text{m}$  and width of  $\approx 18 \mu\text{m}$  was used to investigate the light propagation behavior by accurately shifting the excitation laser spot along the length of the sheet with the collection position fixed at the output end. A typical waveguide photograph is shown in the bottom of Figure 3a, where the rightmost end has a large and bright PL spot when the excitation beam is focused at another end of the sheet. It is observed that the PL intensity of the output end decreases with the increase of the light propagation distance (Figure 3b). The decay coefficient  $\alpha$  can be obtained from the single-exponential fitting  $I_{\text{end}}/I_{\text{body}} = A \exp(-\alpha D)$ , where  $I_{\text{end}}$  is the intensity at emitting site,  $I_{\text{body}}$  is the intensity at body excited site,  $A$  is the ratio of the amount of light escaping from the excitation spot and that of light propagating along the sheet, and  $D$  is the distance between the excited site and the emitting end.<sup>[51]</sup> Thus, decay coefficient for pristine EYS nanosheet,  $\alpha_1$ , is calculated to be  $0.03 \text{ dB } \mu\text{m}^{-1}$  (Figure 3c). The same measurements were conducted for this EYS nanosheet covered with perovskite film as shown in Figure 3d. In stark contrast to the pristine EYS nanosheet, almost no light signal can be observed from the output end of EYS nanosheet (bottom of Figure 3d). The PL intensity collected from the output end of EYS nanosheet covered by perovskite film decreases dramatically with increasing the light propagation distance (Figure 3e). The decay coefficient  $\alpha_2$  of perovskite–EYS hybrid is calculated to be  $0.11 \text{ dB } \mu\text{m}^{-1}$  (Figure 3f), which is threefold higher than that of the pristine EYS nanosheet. Here, the low decay coefficient of pristine EYS nanosheet ( $\alpha_1$ ) suggests a superior light propagation capability

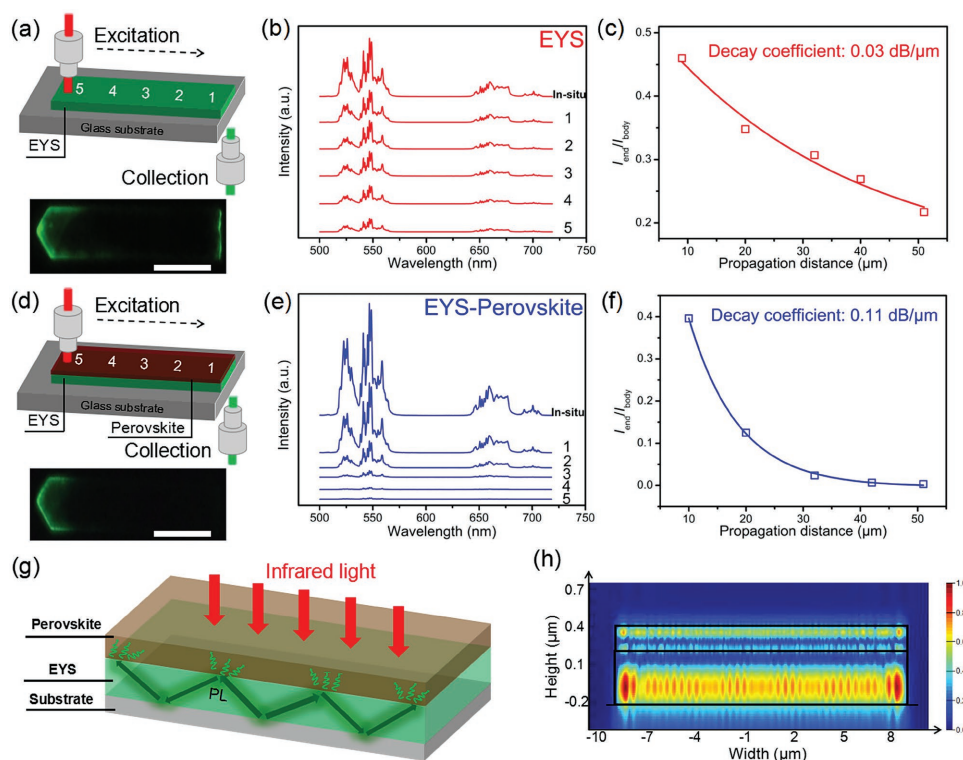


**Figure 3.** Spatially-resolved PL investigations of EYS nanosheet and perovskite–EYS hybrid. a) Schematic diagram of the platform for optical waveguide of EYS nanosheet and a typical PL microscopy image. Scale bar: 20  $\mu\text{m}$ . b) PL collected from the tip of EYS nanosheet as the propagation distance increases. c) The ratio of the intensity  $I_{\text{end}}/I_{\text{body}}$  of pristine EYS against the distance  $D$ . d) Schematic diagram of the platform for optical waveguide of EYS nanosheet covered by perovskite and a typical PL microscopy image. Scale bar: 20  $\mu\text{m}$ . e) PL collected from the tip of EYS covered by perovskite film. f) The ratio of the intensity  $I_{\text{end}}/I_{\text{body}}$  of the hybrid against the distance  $D$ . g) Detailed structure of the EYS waveguide cavity contacted with perovskite. h) Simulated E-field intensity distribution of the crossed junction with guided modes at wavelength of 550 nm as an example.

arising from its planar waveguide geometry,<sup>[51]</sup> single-crystalline nature,<sup>[52,53]</sup> and atomic smooth surface.<sup>[54,55]</sup> After coating with perovskite film, the remarkable increase of the decay coefficient of the perovskite–EYS hybrid ( $\alpha_2$ ) is attributed to the coupling loss of the propagated UC light induced by contacting with higher refractive index perovskite thin film during waveguide.<sup>[56–58]</sup> This high coupling loss of UC light contributes to the efficient energy transfer from EYS nanosheet to perovskite.

In order to shed light on the contribution of the coupling loss of the propagated UC photons, detailed analysis of the PL intensities of EYS and perovskite–EYS hybrid is conducted as shown in Figures S3 and S4 (Supporting Information). It is noteworthy that the output PL intensity of the perovskite–EYS hybrid is remarkably lower than that of the pristine EYS nanosheet after propagating the same distance. For example, at distance of 50  $\mu\text{m}$ , the PL intensity decreases from 52 000 (EYS) to 800 counts (perovskite–EYS hybrid) and is reduced nearly by 98%, which mainly results from the multiple opportunities for energy transfer at perovskite–EYS interfaces during the light propagation within the nanosheet waveguide cavity<sup>[24,25]</sup> and further reveals the highly efficient energy transfer from EYS to perovskite during waveguide. The overall waveguide and energy transfer process are depicted in Figure 3g, where the infrared light induced UC photons can efficiently propagate in the high-quality EYS waveguide cavity. The UC light can be reflected and redirected to the perovskite–EYS interfaces during waveguide,

resulting in the energy transfer from EYS to perovskite through the interfaces. This waveguide process creates multiple opportunities for energy transfer at the interfaces, contributing to a dramatically increased propagation loss within the waveguide mentioned above and consequently leading to enhanced energy transfer efficiency. The energy transfer process is further validated by the simulated E-field intensity distributions in the hybrid structure (Figure 3h). It is observed that the UC light generated in the nanosheet can be evanescently coupled into the perovskite during the propagation at the contact region, which can significantly improve the photoresponsivity of the perovskite–EYS hybrid structure.

Due to the efficient energy transfer from EYS nanosheet to perovskite, a photoelectrical response enhancement at telecommunication band is expected in the hybrid perovskite–EYS nanosheet. The hybrid photodetectors were fabricated using perovskite film and single EYS nanosheet. In our design, as presented in Figure 4a, a p<sup>+</sup>-Si wafer with a 300 nm SiO<sub>2</sub> surface layer was employed as the substrate. Au source/drain electrodes were deposited on the substrate by thermal evaporation after e-beam lithography. Then, the perovskite–EYS nanosheet hybrid photodetector was fabricated using the aforementioned method. It is noted that the EYS nanosheet is not contacted with the source and drain electrodes in the device structure, due to the insulator nature of the silicate material.<sup>[59,60]</sup> No photoresponse of pristine EYS layer was found (Figure S5,

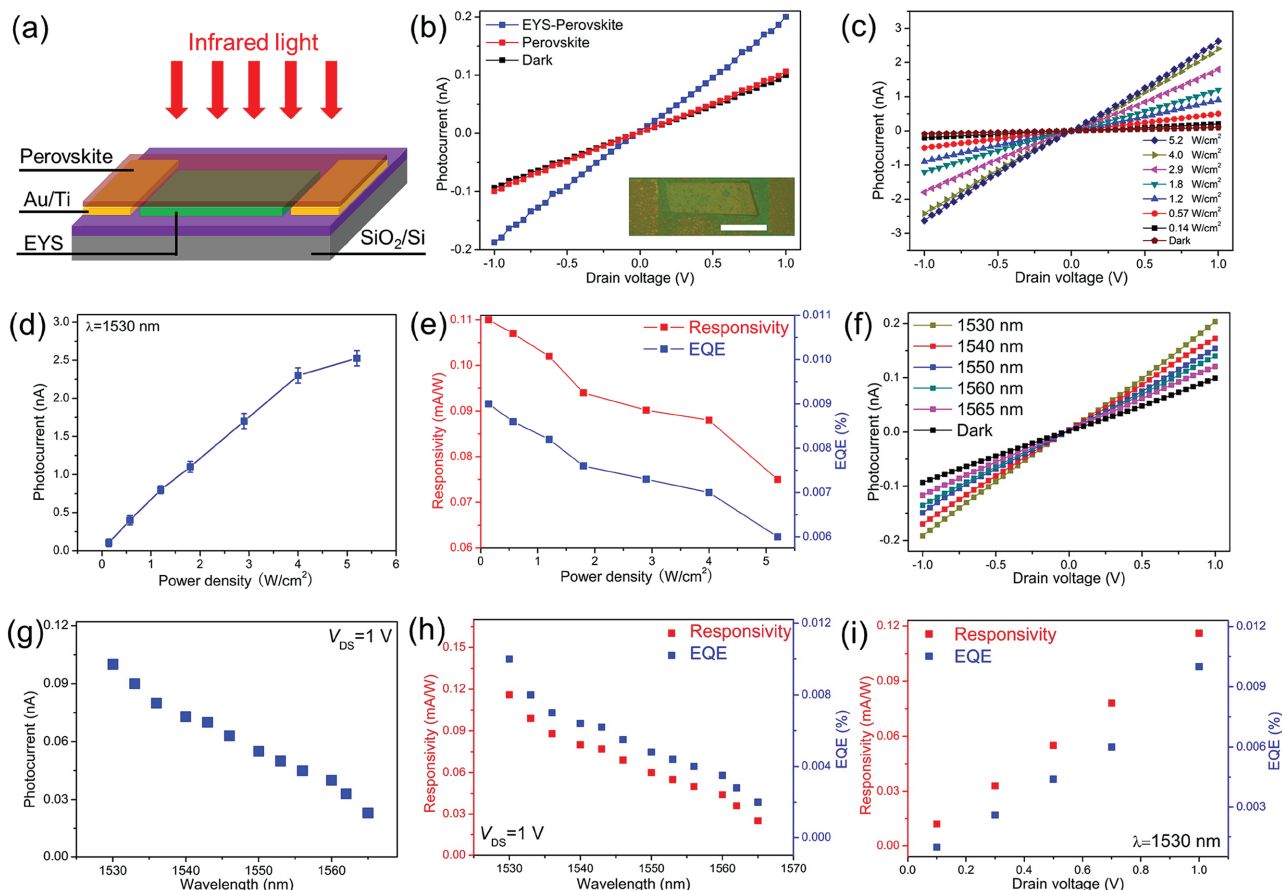


**Figure 4.** Photoresponse performance of perovskite–EYS nanosheet hybrid. a) Schematic of the hybrid device. b)  $I$ – $V$  curves of pristine perovskite and perovskite–EYS nanosheet hybrid in the dark and under 1530 nm light illumination. The inset shows the corresponding optical image. Scale bar: 15  $\mu\text{m}$ . c) Photocurrent–drain voltage plot under various illuminations power densities. d) Photocurrent of the hybrid detector as a function of the power density.  $V_{\text{DS}} = 1$  V. e)  $R$  and EQE versus illumination power density. f)  $I$ – $V$  curves perovskite–EYS hybrid under different illumination wavelength at a fixed power densities of 0.14  $\text{W cm}^{-2}$ . g) Photocurrent as a function of illumination wavelength at an applied bias  $V_{\text{DS}} = 1$  V. h) Responsivity and EQE as a function of illumination wavelength (incident power density: 0.14  $\text{W cm}^{-2}$ ). i) Responsivity and EQE as a function of the bias voltage (incident power density: 0.14  $\text{W cm}^{-2}$ ).

Supporting Information), which further confirms the insulator nature of the EYS nanosheets. The contrasted experiments were conducted to investigate the effects of EYS nanosheet on the photoresponse characteristics of perovskite. The infrared photoresponse of pristine perovskite and perovskite–EYS nanosheet hybrid at illumination power density of 0.14  $\text{W cm}^{-2}$  is shown in Figure 4b. The inset shows the optical image of the device with an active area of  $\approx 650 \mu\text{m}^2$ . It is observed that the pristine perovskite exhibits very low photocurrent under 1530 nm light illumination, which may be attributed to the nonlinear absorption.<sup>[16]</sup> In stark contrast to the pristine perovskite, the perovskite–EYS nanosheet hybrid photodetector shows significantly enhanced photocurrent which is 15 times higher than that of pristine perovskite with same illumination power at drain voltage of 1 V, which validated our previously noted hypothesis. The current–voltage ( $I$ – $V$ ) curves of the hybrid device have been measured in the dark and under illumination with 1530 nm light at different power intensities, as shown in Figure 4c. Under light illumination, the exhibited linear and symmetric  $I$ – $V$  curves of the photodetector indicate ohmic-like contacts between the photoconductors and the electrodes.

Figure 4d shows the illumination power-dependent photocurrent, indicating that the photocurrent increases continuously with the irradiation power due to the enhanced UC luminescence intensity.<sup>[61]</sup> The photoresponsivity ( $R_{\lambda}$ ) and external quantum efficiency (EQE) are important figure-of-merit of photodetectors. The responsivity can be expressed as  $R_{\lambda} = I_{\text{ph}}/PS$ , where  $I_{\text{ph}}$  is the photocurrent,  $P$  is the light power density irradiated on the corresponding photodetector, and  $S$  is the area of the detector. The responsivity is related to the EQE according to the equation:  $\text{EQE} = (R_{\lambda} \times E \times 100)\%$ , where  $R_{\lambda}$  and  $E$  are the photoresponsivity and the incident photon energy, respectively. The responsivity (red dots) and EQE (blue dots) as a function of the illumination power density are summarized in Figure 4e.<sup>[15]</sup> We also measured the dark current noise at different frequencies, as shown in Figure S6 (Supporting Information), which shows the noise power density decreases at a higher frequency, with a small noise current of  $<10^{-24} \text{ A}^2 \text{ Hz}^{-1}$ .

The photoresponse characteristics of the perovskite–EYS nanosheet hybrid photodetector was further investigated over several illumination wavelengths (1530, 1540, 1550, 1560, and 1565 nm), as shown in Figure 4f. The  $I$ – $V$  curves demonstrate

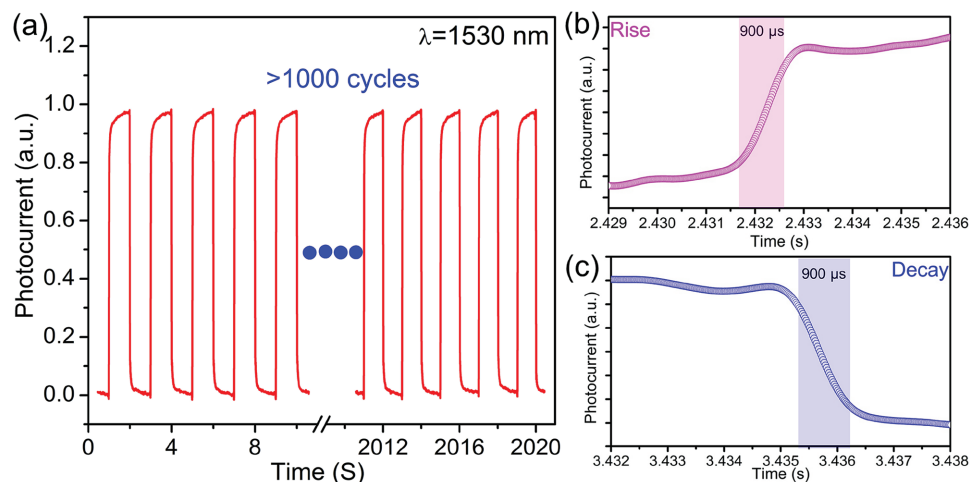


**Figure 5.** Photoswitching characteristics of hybrid photodetector. a) Photoswitching characteristics of the hybrid detector under alternating dark and light illumination at 1530 nm. b) Rise and c) decay times of the hybrid photodetector. All the power density of 1530 nm light and applied bias used here were  $0.14 \text{ W cm}^{-2}$  and 1 V, respectively.

fine wavelength-dependent behaviors of the photodetector.<sup>[11]</sup> The photocurrents as a function of wavelengths at  $V_{DS} = 1 \text{ V}$  are summarized in Figure 4g which indicates full wavelength response at telecommunication band. Figure 4h shows the  $R_\lambda$  (red dots) and EQE (blue dots) as a function of the illumination wavelength. It is observed that the present perovskite–EYS nanosheet hybrid photodetector exhibits a high subbandgap photoresponsivity of  $\approx 0.11 \text{ mA W}^{-1}$  and an EQE of  $\approx 0.01\%$ , which are as high as those of the widely reported microscale silicon-based photodetectors at the same spectral region.<sup>[29–36]</sup> We also plot the responsivity and EQE as a function of the applied  $V_{DS}$  bias (Figure 4i). The detector shows a notable photoresponse even at very low applied bias of 0.1 V with corresponding responsivity of  $0.012 \text{ mA W}^{-1}$ , which is also comparable with the reported values for silicon-based antenna photodetectors.<sup>[35]</sup> The low bias voltages required for operating these composite photodetectors provide the possibility of powering them with miniature button batteries or perovskite solar cells. We attribute the high responsivity of present hybrid device to the high efficiency of UC light harvest mentioned above and superior optoelectronic performance of perovskite. Moreover, the responsivity of the hybrid device could be further enhanced through improving the coupling efficiency and optimizing the gate voltage.

Reliable and fast responses to optical signals is critical for optoelectronic devices. Here, the time-dependent photocurrent response of the hybrid perovskite–EYS nanosheet photodetector was measured, as shown in Figure 5a. We find that the dynamic photoresponse of the detector is highly stable and the signal remains nearly unchanged after more than 1000 cycles of operation, indicating that the achieved devices possess remarkable photoswitching behavior and good stability. The slightly inconstant current under illumination may be attributed to the carrier trapping and scattering at the interfaces.<sup>[62]</sup> The temporal photoresponse of the hybrid photodetector is shown in Figure 5b,c. Sharp responses are observed from which we calculate both the rise and decay times to be  $\approx 900 \mu\text{s}$ . In comparison to the reports in literature, the response speed of our hybrid photodetector presented here is faster by five orders

than those of the silicon-based hot electron photodetectors,<sup>[31–36]</sup> and by one to three orders than most other nonavalanche semiconductor photodetectors at telecommunication wavelengths reported so far.<sup>[37–44]</sup> The present fast response speed is mainly attributed to the very low density of defects and traps within the bandgap of the perovskite material<sup>[63,64]</sup> and simultaneously this outstanding performance of perovskite is preserved in our device architecture. As shown in Figure S7 (Supporting Information), the response time of pristine perovskite under visible light illumination is also  $\approx 900 \mu\text{s}$ , which is comparable with previous report.<sup>[65]</sup> It is noted that both devices, pristine perovskite and perovskite–EYS hybrid, show almost same response speed, indicating no adverse effect of EYS nanosheet on the intrinsic response time of perovskite. In contrast to the previous subbandgap photodetectors, e.g., hot electron-based silicon, in which photoresponsivity were generally improved at the cost of response speed, our proposal significantly enhances the infrared photoresponsivity of perovskite without sacrificing its intrinsic fast response speed.<sup>[26]</sup>

In summary, combining a novel EYS nanosheet waveguide cavity with high-quality methylammonium lead halide film, we have realized, for the first time, efficient perovskite-based near-infrared communication band photodetectors, in taking advantages of the virtues of the both materials. The achieved hybrid waveguide photodetectors exhibit significant improved photoresponse as compared with the pristine perovskite at the full telecommunication wavelengths due to the efficient energy transfer from the EYS waveguide cavity to the perovskite film, with the light response time ( $\approx 900 \mu\text{s}$ ) much faster than those previously reported microscale silicon-based subbandgap photodetectors and nonavalanche semiconductor photodetectors at the same telecommunication wavelengths, simultaneously keeping a comparable responsivity and EQE values. With the advantages of low cost, facile fabrication, and superior performance, the developed microscale perovskite–EYS hybrid waveguide telecommunication photodetectors exhibit great potential for applications in on-chip integrated photonic and optoelectronic devices at telecommunication band.

## Experimental Section

**Sample Fabrication:** The single crystal EYS nanosheets were grown using chemical vapor deposition in a tube reactor. Silicon powder (Alfa Aesar, 99.99%) in a ceramic boat was placed at the center of a quartz tube, which was inserted into a horizontal furnace. The silicon substrate was positioned downstream at a distance of 15 cm from the center of the furnace for the deposition of sample.  $\text{ErCl}_3$  and  $\text{YbCl}_3$  micro beads (Alfa Aesar, 99.99%) in another ceramic boat were loaded upstream and close to the substrate. The tube chamber was evacuated to a pressure below 300 mT and a constant flow of 80 sccm  $\text{Ar-H}_2$  5% mixed gas was introduced as a carrier gas through the quartz tube. The center of the furnace was then heated to 1100 °C, and maintained at this temperature for 100 min. After the growth, the furnace was naturally cooled to room temperature. The perovskite films were grown using the two-step solution process.  $\text{PbI}_2$  layer with the thickness of 80 nm was deposited on the substrates through thermal evaporation. The  $\text{CH}_3\text{NH}_3\text{I}$  solution was prepared by dissolving  $\text{CH}_3\text{NH}_3\text{I}$  into anhydrous isopropyl alcohol. After fully dissolved, the  $\text{CH}_3\text{NH}_3\text{I}$  solution was spin-coated onto the  $\text{PbI}_2$  covered substrate. Finally, the substrate was annealed on a hot plate at 100 °C for 2 h.

**Materials Characterization:** SEM micrographs were taken using a Zeiss instrument (Sigma HD-01-61). TEM study was performed on a Tecnai G<sup>2</sup> (F20 S-TWIN). XRD patterns were recorded using a Rigaku diffractometer (D/MAX 2500). The PL measurement were characterized by a confocal  $\mu$ -PL system (WITEC, alpha-300). The absorption spectrum was recorded using a Perkin-Elmer spectrometer (Lambda 25 UV/VIS).

**Numerical Simulation:** The numerical simulation of the hybrid crossed junction were carried out using the finite difference time domain method for solving Maxwell's equations. A 190 nm thickness, 18  $\mu\text{m}$  width perovskite film placed atop a 400 nm thickness, 18  $\mu\text{m}$  width EYS nanosheet which based on the silica substrate was selected as numerical model (Figure 3a; Figure S8, Supporting Information). The 550 nm light was launched into EYS channel and the E-field intensity distributions of the guided modes in the crossed junction were calculated.

**Photodetector Fabrication and Characterization:**  $\text{SiO}_2/\text{p}^+\text{-Si}$  wafer was used as the starting substrate. Photolithography was employed to define the source and drain electrodes. The Au (50 nm) was deposited onto the wafer using a thermal evaporator. The EYS nanosheet with thickness of 400 nm was then transferred onto the substrate between source and drain electrodes.  $\text{PbI}_2$  (80 nm) film was thermally sublimed onto  $\text{SiO}_2/\text{Si}$  substrate.  $\text{CH}_3\text{NH}_3\text{I}$  (15 mg  $\text{mL}^{-1}$ ) solution was spin-coated onto  $\text{PbI}_2$  layer at 3000 rpm for 30 s. A postannealing process at 100 °C is applied for 2 h to fully crystallize the perovskite film. Optoelectronic properties were monitored with a Keithley semiconductor parameter analyser (4200-SCS), oscilloscope, and a near-infrared tunable diode laser.

## Supporting Information

Supporting Information is available from the Wiley Online Library or from the author.

## Acknowledgements

X.Z., S.Y., and H.Z. contributed equally to this work as first authors. The authors are grateful to the National Natural Science Foundation of China (Nos. 11374092, 61474040, 61574054, 61505051, 61635001), the Aid Program for Science and Technology Innovative Research Team in Higher Educational Institutions of Hunan Province, and the Hunan Provincial Science and Technology Department (Nos. 2014FJ2001, 2014TT1004).

Received: August 19, 2016  
Revised: November 5, 2016  
Published online:

- [1] H. M. Zhu, Y. P. Fu, F. Meng, X. X. Wu, Z. Z. Gong, Q. Ding, M. V. Gustafsson, M.T. Trinh, S. Jin, X. Y. Zhu, *Nat. Mater.* **2015**, *14*, 636.
- [2] J. Burschka, N. Pellet, S. J. Moon, R. Humphry-Baker, P. Gao, M. K. Nazeeruddin, M. Grätzel, *Nature* **2013**, *499*, 316.
- [3] S. T. Ha, C. Shen, J. Zhang, Q. H. Xiong, *Nat. Photonics* **2016**, *10*, 115.
- [4] M. I. Saidaminov, V. Adinolfi, R. Comin, A. L. Abdelhady, W. Peng, I. Dursun, M. J. Yuan, S. Hoogland, E. H. Sargent, O. M. Bakr, *Nat. Commun.* **2015**, *6*, 8724.
- [5] K. Y. Yan, M. Z. Long, T. K. Zhang, Z. H. Wei, H. N. Chen, S. H. Yang, J. B. Xu, *J. Am. Chem. Soc.* **2015**, *137*, 4460.
- [6] S. Chen, C. J. Teng, M. Zhang, Y. R. Li, D. Xie, G. Q. Shi, *Adv. Mater.* **2016**, *28*, 5969.
- [7] M. I. Saidaminov, M. A. Haque, M. Savoie, A. L. Abdelhady, N. Cho, I. Dursun, U. Buttner, E. Alarousu, T. Wu, O. M. Bakr, *Adv. Mater.* **2016**, *28*, 8144.
- [8] R. Dong, Y. J. Fang, J. Chae, J. Dai, Z. G. Xiao, Q. F. Dong, Y. B. Yuan, A. Centrone, X. C. Zeng, J. S. Huang, *Adv. Mater.* **2015**, *27*, 1912.
- [9] M. S. Long, E. F. Liu, P. Wang, A. Y. Gao, H. Xia, W. Luo, B. G. Wang, J. W. Zeng, Y. J. Fu, K. Xu, W. Zhou, Y. Y. Lv, S. H. Yao, M. H. Lu, Y. F. Chen, Z. H. Ni, Y. M. You, X. A. Zhang, S. Q. Qin, Y. Shi, W. D. Hu, D. Y. Xing, F. Miao, *Nano Lett.* **2016**, *16*, 2254.
- [10] J. Wang, R. R. Deng, M. A. Macdonald, B. L. Chen, J. K. Yuan, F. Wang, D. Z. Chi, T. S. A. Hor, P. Zhang, G. K. Liu, Y. Han, X. G. Liu, *Nat. Mater.* **2014**, *13*, 157.
- [11] H. Higuchi, M. Takahashi, Y. Kawamoto, K. Kadono, T. Ohtsuli, N. Peyghambarian, N. Kitamura, *J. Appl. Phys.* **1998**, *83*, 19.
- [12] G. Y. Chen, T. Y. Ohulchanskyy, A. Kachynski, H. Ågren, P. N. Prasad, *ACS Nano* **2011**, *5*, 4981.
- [13] L. T. Su, S. K. Karuturi, J. S. Luo, L. J. Liu, X. F. Liu, J. Guo, T. C. Sum, R. Deng, H. J. Fan, X. G. Liu, A. L. Y. Tok, *Adv. Mater.* **2013**, *25*, 1603.
- [14] X. Y. Huang, S. Y. Han, W. Huang, X. G. Liu, *Chem. Soc. Rev.* **2013**, *42*, 173.
- [15] Y. Tong, X. Y. Zhao, M. C. Tan, R. Zhao, *Sci. Rep.* **2015**, *5*, 16761.
- [16] C. L. Yan, A. Davand, F. Rosei, D. F. Perepichka, *J. Am. Chem. Soc.* **2010**, *132*, 8868.
- [17] Y. Zhou, S. T. Han, X. Chen, F. Wang, Y. B. Tang, V. A. L. Roy, *Nat. Commun.* **2014**, *5*, 4720.
- [18] H. Jia, C. Ping, C. Xu, J. J. Zhou, X. W. Sang, J. C. Wang, C. Liu, X. F. Liu, J. R. Qiu, *J. Mater. Chem. A* **2015**, *3*, 5917.
- [19] M. He, X. C. Pang, X. Q. Liu, B. B. Jiang, Y. J. He, H. Snaith, Z. Q. Lin, *Angew. Chem., Int. Ed.* **2016**, *128*, 4352.
- [20] Y. Yao, E. Brueckner, L. F. Li, R. Nuzzo, *Energy Environ. Sci.* **2013**, *6*, 3071.
- [21] J. Yoon, L. F. Li, A. V. Semichaevsky, J. H. Ryu, H. T. Johnson, R. G. Nuzzo, J. A. Rogers, *Nat. Commun.* **2011**, *2*, 343.
- [22] S. F. H. Correia, V. D. Z. Bermudez, S. J. L. Ribeiro, P. S. André, R. A. S. Ferreira, L. D. Carlos, *J. Mater. Chem. A* **2014**, *2*, 5580.
- [23] M. J. Currie, J. K. Mapel, T. D. Heidel, S. Goffri, M. A. Baldo, *Science* **2008**, *321*, 226.
- [24] B. Weintraub, Y. G. Wei, Z. L. Wang, *Angew. Chem., Int. Ed.* **2009**, *48*, 8981.
- [25] Y. G. Wei, C. Xu, S. Xu, C. Li, W. Z. Wu, Z. L. Wang, *Nano Lett.* **2010**, *10*, 2092.
- [26] X. T. Gan, R. J. Shiu, Y. D. Gao, I. Meric, T. F. Heinz, K. Shepard, J. Hone, S. Assefa, D. Englund, *Nat. Photonics* **2013**, *7*, 883.
- [27] M. Furchi, A. Urich, A. Pospischil, G. Lilley, K. Unterrainer, H. Detz, P. Klang, A. M. Andrews, W. Schrenk, G. Strasser, T. Mueller, *Nano Lett.* **2012**, *12*, 2773.
- [28] X. M. Wang, Z. Z. Cheng, K. Xu, H. K. Tsang, J. B. Xu, *Nat. Photonics* **2013**, *7*, 888.

- [29] J. P. Mailoa, A. J. Key, C. B. Simmons, D. Hutchison, J. Mathews, J. T. Sullivan, D. Recht, M. T. Winkler, J. S. Williams, J. M. Warrender, P. D. Persans, M. J. Aziz, T. Buonassisi, *Nat. Commun.* **2014**, *5*, 3011.
- [30] I. Goykhman, B. Desiatov, J. Khurgin, J. Shappir, U. Levy, *Nano Lett.* **2011**, *11*, 2219.
- [31] M. L. Brongersma, N. J. Halas, P. Nordlander, *Nat. Nanotechnol.* **2015**, *10*, 25.
- [32] M. A. Nazirzadeh, F. B. Atar, B. B. Turgut, A. K. Okyay, *Sci. Rep.* **2014**, *4*, 7103.
- [33] A. Sobhani, M. W. Knight, Y. M. Wang, B. Zheng, N. S. King, L. V. Brown, Z. Y. Fang, P. Nordlander, N. J. Halas, *Nat. Commun.* **2013**, *4*, 1643.
- [34] K. T. Lin, H. L. Chen, Y. S. Lai, C. C. Yu, *Nat. Commun.* **2014**, *5*, 3288.
- [35] M. W. Knight, H. Sobhani, P. Nordlander, N. J. Halas, *Science* **2011**, *332*, 702.
- [36] K. Wu, Y. H. Zhan, S. L. Wu, J. J. Deng, X. F. Li, *Appl. Phys. Lett.* **2015**, *118*, 063101.
- [37] Z. X. Wang, M. Safdar, C. Jiang, J. He, *Nano Lett.* **2012**, *12*, 4715.
- [38] L. Ma, W. Hu, Q. L. Zhang, P. Y. Ren, X. J. Zhuang, H. Zhou, J. Y. Xu, H. L. Li, Z. P. Shan, X. X. Wang, L. Liao, H. Q. Xu, A. L. Pan, *Nano Lett.* **2014**, *14*, 694.
- [39] H. Tan, C. Fan, L. Ma, X. H. Zhang, P. Fan, Y. K. Yang, W. Hu, H. Zhou, X. J. Zhuang, X. L. Zhu, A. L. Pan, *Nano-Micro Lett.* **2016**, *8*, 29.
- [40] K. N. Zhang, T. N. Zhang, G. H. Cheng, T. X. Li, S. X. Wang, W. Wei, X. H. Zhou, W. W. Yu, Y. Sun, P. Wang, D. Zhang, C. G. Zeng, X. J. Wang, W. D. Hu, H. J. Fan, G. Z. Shen, X. Chen, X. F. Duan, K. Chang, N. Dai, *ACS Nano* **2016**, *10*, 3852.
- [41] X. D. Wang, P. Wang, J. L. Wang, W. D. Hu, X. H. Zhou, N. Guo, H. Huang, S. Sun, T. Lin, M. H. Sun, L. Liao, A. Q. Jiang, J. L. Sun, X. J. Meng, X. S. Chen, W. Lu, J. H. Chu, *Adv. Mater.* **2015**, *27*, 6575.
- [42] D. Kufer, I. Nikitskiy, T. Lasanta, G. Navickaite, F. H. L. Koppens, G. Konstantatos, *Adv. Mater.* **2015**, *27*, 176.
- [43] Z. F. Zhu, Y. S. Zou, W. D. Hu, Y. B. Li, Y. Gu, B. Q. Cao, N. Guo, L. Wang, J. Z. Song, S. L. Zhang, H. S. Gu, H. B. Zeng, *Adv. Funct. Mater.* **2016**, *26*, 1793.
- [44] W. Y. Liu, J. S. Lee, D. V. Talapin, *J. Am. Chem. Soc.* **2013**, *135*, 1349.
- [45] X. X. Wang, X. J. Zhuang, S. Yang, Y. Chen, Q. L. Zhang, X. L. Zhu, H. Zhou, P. F. Guo, J. W. Liang, Y. Huang, A. L. Pan, X. F. Duan, *Phys. Rev. Lett.* **2015**, *115*, 027403.
- [46] A. L. Pan, L. J. Yin, Z. C. Liu, M. H. Sun, R. B. Liu, P. L. Nicholas, Y. G. Wang, C. Z. Ning, *Opt. Mater. Express* **2011**, *1*, 1202.
- [47] B. R. Sutherland, S. Hoogland, M. M. Adachi, P. Kanjanboos, C. T. O. Wong, J. J. McDowell, J. X. Xu, O. Voznyy, Z. J. Ning, A. J. Houtepen, E. H. Sargent, *Adv. Mater.* **2014**, *27*, 53.
- [48] C. Ma, Y. M. Shi, W. J. Hu, M. H. Chiu, Z. X. Liu, A. Bera, F. Li, H. Wang, L. L. Li, T. Wu, *Adv. Mater.* **2016**, *28*, 3683.
- [49] L. L. Wang, C. McCleese, A. Kovalsky, Y. X. Zhao, C. Burda, *J. Am. Chem. Soc.* **2014**, *136*, 12205.
- [50] S. Z. Bisri, T. Takenobu, Y. Yomogida, H. Shimotani, T. Yamao, S. Hotta, Y. Iwasa, *Adv. Funct. Mater.* **2009**, *19*, 1728.
- [51] W. G. Zhu, R. H. Zheng, X. L. Fu, H. B. Fu, Q. Shi, Y. G. Zhen, H. L. Dong, W. P. Hu, *Angew. Chem., Int. Ed.* **2015**, *54*, 6785.
- [52] A. Ikesue, Y. L. Ang, *Nat. Photonics* **2008**, *2*, 721.
- [53] J. Riedrich-Möller, L. Kipfstuhl, C. Hepp, E. Neu, C. Pauly, F. Mücklich, A. Baur, M. Wandt, S. Wolff, M. Fishcer, S. Gsell, M. Schreck, C. Becher, *Nat. Nanotechnol.* **2012**, *7*, 69.
- [54] Y. Zou, D. N. Zhang, H. T. Lin, L. Li, L. Moreel, J. Zhou, Q. Y. Du, O. Ogbuu, S. Danto, J. David Musgraves, K. Richardson, K. D. Dobson, R. Birkmire, J. J. Hu, *Adv. Opt. Mater.* **2014**, *2*, 478.
- [55] R. H. Ding, L. Tsang, H. Braunisch, *IEEE Trans. Microwave Theory Tech.* **2009**, *57*, 1216.
- [56] P. Löper, M. Stuckelberger, B. Niesen, J. Werner, M. Filipic, S. J. Moon, J. H. Yum, M. Topič, S. D. Wolf, C. Ballif, *J. Phys. Chem. Lett.* **2015**, *6*, 66.
- [57] I. A. Bondar, *Ceram. Int.* **1982**, *8*, 83.
- [58] M. Miritello, R. L. Savio, P. Cardile, F. Priolo, *Phys. Rev. B* **2010**, *81*, 041411.
- [59] Y. Yin, W. J. Xu, F. Wei, G. Z. Ran, G. G. Qin, Y. F. Shi, Q. G. Yao, S. D. Yao, *J. Phys. D: Appl. Phys.* **2010**, *43*, 335102.
- [60] S. Y. Chang, M. I. Jeong, S. V. J. Chandra, Y. B. Lee, H. B. Hong, V. R. Reddy, C. J. Choi, *Mater. Sci. Semicond. Process.* **2008**, *11*, 122.
- [61] B. Dong, B. S. Cao, Y. Y. He, Z. Liu, Z. P. Li, Z. Q. Feng, *Adv. Mater.* **2012**, *24*, 1987.
- [62] J. P. Lu, A. Carvalho, H. W. Liu, S. X. Lim, A. H. C. Neto, C. H. Sow, *Angew. Chem.* **2016**, *128*, 12124.
- [63] W. J. Yin, T. T. Shi, Y. F. Yan, *Adv. Mater.* **2014**, *26*, 4653.
- [64] L. T. Dou, Y. Yang, J. B. You, Z. R. Hong, W. H. Chang, G. Li, Y. Yang, *Nat. Commun.* **2014**, *5*, 5404.
- [65] W. Z. Wang, H. T. Xu, J. Cai, J. B. Zhu, C. W. Ni, F. Hong, Z. B. Fang, F. Z. Xu, S. W. Cui, R. Xu, L. J. Wang, F. Xu, J. Huang, *Opt. Express* **2016**, *24*, 841.